








A two-hump spectrum in the prompt emission of GRB 240825A

HAI-MING ZHANG ¹, ZI-QI WANG ¹, CUI-YUAN DAI ^{2,3}, YI-YUN HUANG ^{2,3}, RUO-YU LIU ^{2,3}, EN-WEI LIANG ¹,
AND XIANG-YU WANG ^{2,3}

¹*Guangxi Key Laboratory for Relativistic Astrophysics, School of Physical Science and Technology, Guangxi University, 530004 Nanning, Guangxi, China; hmzhang@gxu.edu.cn*

²*School of Astronomy and Space Science, Nanjing University, Nanjing 210023, China; xywang@nju.edu.cn*

³*Key laboratory of Modern Astronomy and Astrophysics (Nanjing University), Ministry of Education, Nanjing 210023, China*

ABSTRACT

An extra hard spectral component that extends to GeV energies, in addition to the typical sub-MeV Band component, appears in several gamma-ray burst (GRBs) detected by *Fermi* Large Area Telescopes (LAT). Only in one case (i.e., GRB 090926A), a spectral break feature at the high energy end is identified in the extra hard component, but the photon counts are not enough to distinguish between the cutoff model and the broken power law model for the spectral break. In this work, we report the detection of an extra hard component showing the spectral break in GRB 240825A. We find that a broken power-law model fits the spectral data of the extra component better than a single power-law with an exponential cutoff in the time resolved spectrum for the second emission pulse, with a break at about 50 MeV. This spectral feature disfavors the gamma-ray opacity to pair creation as the origin of the spectral break, but points to an intrinsic peak for the extra component. The low ratio between the peak of the extra hard component and that of the Band component challenges the synchrotron self-Compton origin for the extra component. Alternative scenarios, such as the inverse Compton scattering of the photosphere emission, are discussed. In addition, we find a clear transition from the prompt emission to afterglow emission at GeV energies in GRB 240825A, manifested by a temporal steep decay and an unique spectral evolution.

Keywords: Gamma-ray bursts (629) — High energy astrophysics (739)

1. INTRODUCTION

Gamma-ray bursts (GRBs) are the most luminous transients in the universe. The emission of GRBs consists of two stages: the first brief and intense flash, called the prompt emission, and the long-lived afterglow. The long-lived afterglow is thought to result from external shocks caused by the interaction of the relativistic jets with the ambient medium at large radii (e.g., Kumar & Zhang 2015). The afterglow emission spans a wide range of frequencies of electromagnetic wave, interpreted as synchrotron radiation or inverse-Compton emission from relativistic electrons that are accelerated by the external shock.

While the origin of the long-lived afterglow is established, the radiation origin and dissipation mechanism of the prompt emission is not well unknown. The spectrum of the prompt emission is usually described by an empirical function (called the Band function) composed by two smoothly connected power-laws (PLs), with indices $\alpha \sim -1$ and $\beta \sim -2.5$ at low and high energies,

respectively (Band et al. 1993). Two leading models proposed could roughly explain the general shape of the spectra. One model invokes synchrotron radiation of the electrons accelerated in the energy dissipation regions (internal shocks or magnetic reconnection sites) to account for the prompt emission. However, for a typical GRB environment the electrons are in the so-called "fast-cooling" regime that leads to $\alpha = -1.5$ for the low-energy spectral index, which is too "soft" to account for the data (the so-called synchrotron line-of-death problem). Various scenarios have been proposed to harden the spectrum from the fast-cooling $\alpha = -1.5$ to the typical $\alpha = -1$ (e.g., Pe'er & Zhang 2006; Uhm & Zhang 2014; Daigne et al. 2011). Recently, some studies found that using the synchrotron model spectrum itself (rather than the Band function) to fit the data directly was successful (Burgess et al. 2014; Zhang et al. 2016; Burgess et al. 2019). Another model invokes quasi-thermal emission from a relativistic fireball (i.e., the photosphere emission model), where the thermal energy stored in the

jet can be radiated as prompt emission at the Thomson photosphere (e.g., Mészáros & Rees 2000; Ryde et al. 2010; Gao & Zhang 2015). The inclusion of a quasi-thermal component can significantly harden the GRB spectra.

In some LAT-detected GRBs, such as GRB 080916C, GRB 090510, GRB 090902B, GRB 090926A, GRB 110731A, and GRB 130427A, a second, harder spectral component (in addition to the common Band component) has been clearly identified during the prompt phase (see Nava (2018) for a review). The quality of the data usually does not allow a detailed study of its spectral shape, and a simple PL provides an acceptable fit to the extra component. Typically, the PL photon index of this component is greater than -2, that is harder than the high-energy part of the prompt keV–MeV spectrum. In one case (GRB 090926A), a high-energy spectral cutoff (or break) is found (Ackermann et al. 2011). The spectrum can be modeled by a Band component adding a PL with an exponential cutoff (CPL), both in the time-integrated analysis and in the time resolved spectrum, and the cutoff energy is located at ~ 1.4 GeV in the time-integrated spectrum. The data can also be fitted with a broken power-law model and the significance of the fit was close to that found using the CPL model, so that the two models can not be distinguished. The cutoff/break has been interpreted in terms of gamma-ray opacity to pair creation and used to estimate the bulk Lorentz factor of the outflow (Ackermann et al. 2011).

There are several theoretical models for the origin of the extra spectral component. In the internal shock synchrotron emission scenario, an extra hard component during the prompt phase can arise from synchrotron self-Compton (SSC) radiation, i.e. inverse Compton (IC) scattering of the Band component (e.g., Bošnjak & Daigne 2014). In the photospheric emission model of the Band component, the extra component could be due to IC scattering of the photospheric emission by relativistic electrons in the internal shock/dissipation region at large radius above the photosphere (Beloborodov 2009; Gao et al. 2009; Ryde et al. 2010; Toma et al. 2011). Hadronic models, for example, synchrotron radiation from protons or photohadronic interactions, are also suggested to explain the extra hard component (e.g., Asano et al. 2009). The main difficulty of hadronic models, however, is that an extremely high energy budget is required (Wang et al. 2009).

In this paper, we report on the analysis of *Fermi* GBM and LAT data of a bright GRB 240825A. The spectral analysis of the prompt emission for this burst shows an extra hard component peaking at about 50 MeV, apart from the canonical Band function. The peak energy of

the extra component is one order of magnitude of lower than that in GRB 090926A. We also find that the broken power-law model fits the spectral data better than the CPL model in some time intervals of the prompt emission. This gives us new insight in the origin of the extra hard components in GRBs. In Section 2, we give a brief summary of the observations of GRB 240825A by the GBM and LAT, as well as the follow-up multi-wavelength observations. In Section 3, we report the temporal analysis of the GBM and LAT data. We show the spectral analysis of the burst in Section 4 and present the result of the LAT extended emission in Section 5. We then discuss these results in Section 6 and give a summary in Section 7.

2. OBSERVATIONS

At 15:53:00 UT (T_0) on 25 August 2024, the GBM triggered on and localized GRB 240825A at (R.A., decl.) = (341°.6, 5°.9) in J2000 coordinates (Fermi GBM Team 2024). GRB 240825A is also triggered by the Swift Burst Alert Telescope (BAT; Gupta et al. (2024)), GECAM-B (Wang et al. 2024) and *Fermi*-LAT (Di Lalla et al. 2024; Sharma et al. 2024). The GBM light curve have many overlapping short pulses with a duration (T_{90}) of about 4 s in 50-300 keV (Sharma et al. 2024). Using the conical Band function to model the spectrum, the event fluence (10-1000 keV) in the time interval from $T_0 + 0.96$ s to $T_0 + 6.85$ s is $(1.01 \pm 0.01) \times 10^{-4}$ erg cm $^{-2}$ (Sharma et al. 2024). Using the X-shooter spectrograph, Very Large Telescope (VLT) observations determined a redshift for GRB 240825A of $z = 0.659$ (Martin-Carrillo et al. 2024). GRB 240825A is also observed by many other facilities, including optical (Jiang et al. 2024; Dutton et al. 2024; Odeh & Guessoum 2024; Zhang et al. 2024; Lipunov et al. 2024; Li et al. 2024; SVOM/C-GFT Team et al. 2024; Cheng et al. 2024), near-infrared (NIR) (Brivio et al. 2024; Guiffreda et al. 2024), X-ray (Evans et al. 2024) and gamma-ray (Frederiks et al. 2024).

3. LIGHT CURVE

The *Fermi* Gamma-ray Space Telescope hosts two instruments, e.g., GBM and LAT. The GBM has 12 sodium iodide (NaI) and two bismuth germanate (BGO) scintillation detectors, covering the energy range 8 keV–40 MeV (Meegan et al. 2009). The LAT is a pair conversion telescope covering the range from below 20 MeV to more than 300 GeV (Atwood et al. 2009). We downloaded GBM data and LAT extended type data of GRB 240825A from the *Fermi* GBM pub-

lic data archive¹ and the *Fermi* Science Support Center², respectively. For the GBM data, GRB 240825A produced large signals in two NaI detectors and one BGO detector, namely NaI₆, NaI₇ and BGO₁. For the LAT data, only the data within a 20° region of interest (ROI) centered on the position of GRB 240825A are considered for the analysis. The publicly available Pass 8 (P8R3) LAT data for GRB 240825A was processed using the *fermitools* (v2.2.0) package, distributed by the Fermi Collaboration. Events of the “Transient” class (*P8R3_TRANSIENT020_V3*; using for the time before $T_0 + 400$ s) and “Source” class (*P8R3_SOURCE_V3*; using for the time after $T_0 + 400$ s) were selected. We assumed a power-law spectrum in the 0.1–100 GeV energy range, with accounting for the diffuse Galactic and extragalactic backgrounds.

The light curves in several energy bands of GRB 240825A, as observed by GBM and LAT, are shown in Figure 1. Because of the energy-dependent temporal structure of the light curve, we divided the light curve into four time intervals (a, b, c, and d) delineated by the vertical lines (Figure 1). The boundaries of time intervals with $T_0 + [0.529, 1.901, 3.915, 5.831, 10.072]$ s are obtained from the bayesian block analysis. The GRB light curve at low energy has two bright peaks, one between 0 and 1.901 s after the trigger (interval a) and one between 1.901 s and 3.915 s (interval b). The two peaks are distinct in the BGO light curve but less so in the NaI. Interestingly, the light curves show that the onset of high-energy GBM emission (10–40 MeV) and the LAT emission (0.1–100 GeV) are delayed by ~ 0.6 s with respect to the low-energy GBM emission (< 10 MeV), similar to other LAT GRBs, e.g., GRB 080825C (Abdo et al. 2009a), GRB 080916C (Abdo et al. 2009b), GRB 081024B (Abdo et al. 2010), GRB 090217A (Ackermann et al. 2010a), GRB 090510 (Abdo et al. 2009c; Ackermann et al. 2010b), GRB 090902B (Abdo et al. 2009d) and GRB 090926A (Ackermann et al. 2011).

After applying the standard selection cuts and background subtraction in the first 10 s after the trigger, the total number of LAT counts is 284, and for the 2000 s after the trigger, the total number is 324. In the panel 5 of Figure 1, we show the photons with energy greater than 100 MeV that have a high association probability ($> 95\%$) with GRB 240825A. One can see that, most of the photons are low-energy events (< 1 GeV), and only 4 events have energies ≥ 1 GeV in the first 10 s after the trigger. The highest energy photon is a 40.2 GeV

event, which is observed at $T_0 + 239.19$ s within $0^\circ.04$ from the LAT position of this GRB.

4. SPECTRAL ANALYSIS OF THE PROMPT EMISSION

We select GBM NaI data of NaI₆ and NaI₇ from 8 keV to 800 keV, as well as BGO₁ data from 200 keV to 40 MeV. For LAT photons, we selected the events for the energies from 100 MeV to 100 GeV using the unbinned analysis method. Because the LAT emission is mainly dominated by the afterglow emission during the time interval $T_0 + [5.831, 10.072]$ s (see section 5), we use the interval $T_0 + [0.529, 5.831]$ s for the time-integrated joint spectral analysis of the GBM and LAT data. The spectral analysis is performed using XSPEC (version 12.13.0c; Arnaud 1996). Firstly, we use a canonical Band function (Band et al. 1993) for the time-integrated joint spectral analysis. We find that the Band function can not described well the spectrum, as the BGO data and LAT data deviate from the Band function and the goodness of fit is $\text{PGSTAT}/\text{dof} = 648.41/362$ (dof is the degrees of the freedom). Comparing the BGO data and LAT data, the spectrum shows a cutoff tendency in the high energy band. Thus, we consider to add an extra power-law component with an exponential cutoff (CPL) to fit the data. The CPL function is expressed as

$$N(E) = BE^{\alpha_1} \exp\left(-\frac{E}{E_{\text{cut}}}\right), \quad (1)$$

where B is the normalization in units of photons $\text{s}^{-1} \text{cm}^{-2} \text{keV}^{-1}$, α_1 is the power-law index and E_{cut} is the e-folding energy. We obtain $E_{\text{cut}} = 50.74_{-16.11}^{+29.64}$ MeV and $\alpha_1 = 1.09_{-0.38}^{+0.26}$ for the time-integrated spectrum. The PGSTAT value for the Band+CPL model is 574.96, which improves by 73.45 compared to the Band-only model. Considering the model complexity and the different numbers of free parameters, we employ the Bayesian information criterion (BIC; Schwarz 1978) to compare the goodness of fit of the two models. The BIC value of the Band+CPL model is 616.28, which is lower than that of the Band model. The BIC difference (ΔBIC) of these two models is 55.74, which indicates very strong evidence against the Band model³.

¹ <https://heasarc.gsfc.nasa.gov/FTP/fermi/data/gbm/daily/>

² <https://fermi.gsfc.nasa.gov>

³ In this work, we accepted a more complex model to be preferred over a simpler one whenever the difference in BIC is greater than 4. The detailed strength of the evidence against the model with a higher BIC value can be seen in Nunes et al. (2017).

We also try to fit the data with the Band function plus a broken power-law (BPL) model

$$N(E) = \begin{cases} CE^{\alpha_l} & \text{if } E \leq E_{\text{break}} \\ CE_{\text{break}}^{\alpha_l - \alpha_h} \left(\frac{E}{1\text{keV}}\right)^{\alpha_h} & \text{if } E > E_{\text{break}}, \end{cases} \quad (2)$$

where E_{break} is the break energy, α_l and α_h are the low- and high-energy power-law photon indices, respectively. The fit with an extra BPL gives a break energy $E_{\text{break}} = 35.71_{-15.08}^{+14.29}$ MeV, a low-energy photon index of $\alpha_l = -1.23_{-0.12}^{+0.31}$ and a high-energy photon index of $\alpha_h = -3.00_{-0.44}^{+0.36}$. The BIC difference between the Band+CPL model and the Band+BPL model is $\Delta\text{BIC} = 4.24$, indicating positive evidence against the the Band+CPL model. In Figure 2, we show the spectral fits and residuals for the Band+CPL model (left panel) and the Band+BPL model (right panel), respectively. The residuals of the fitting show that the Band+BPL model fits the LAT data better than the Band+CPL model. The fitting results of the three models are listed in Table 1.

We note that the BGO data deviate slightly from the Band+BPL model at 4 – 10 MeV. This narrow bump feature is reminiscent of the spectral line at about 10 MeV seen in GRB 221009A (Ravasio et al. 2024). We try to add a Gaussian component to model the excess flux observed at MeV energies, yielding $E_{\text{gauss}} = 7.57_{-0.28}^{+0.20}$ MeV, $\sigma_{\text{gauss}} = 0.19_{-0.19}^{+0.35}$ MeV and a statistics for the fitting $\text{PGSTAT}/\text{dof} = 538.90/355$. The BIC difference between the Band+BPL model and the Band+BPL+Guass model is $\Delta\text{BIC} = 8.21$, supporting the presence of the Gaussian component. However, we have not tested whether this signal could be caused by instrument effects and background selection. Since this component does not affect the result of the extra component that locates at high energy, we leave a detailed analysis about this Gaussian component in future work.

We then perform time-resolved joint spectral analyses of the GBM and LAT data. As seen in Figure 1, the LAT emission is significantly delayed relative to the keV-MeV prompt emission recorded by the GBM, we divide the interval a into two segments, one without LAT emission (interval a_1) and the other with LAT emission (interval a_2). For the interval a_1 , the spectral data is well fitted by a Band function, while for the interval a_2 , the preferred model is Band+CPL model, which improves the fit relative to the Band function with $\Delta\text{BIC} = 59.71$. For the whole interval a, the Band+CPL model is the preferred model. For the interval b, the preferred model is Band+BPL model. Compared to Band+CPL model, the Band+BPL model improves the fit with $\Delta\text{BIC} = 15.00$. The break energy

of the BPL component is at $E_{\text{break}} = 51.22_{-12.68}^{+12.19}$ MeV. The comparison for the two model fits is shown in Figure 3. In interval c, the preferred model is Band+CPL model and the best-fit parameters of the extra CPL model are $E_{\text{cut}} = 37.49_{-15.01}^{+20.08}$ MeV and $\alpha_1 = -1.24_{-0.49}^{+0.27}$. Due to the low statistics of the LAT data for interval d, the parameters are not very well constrained for Band+CPL or Band+BPL models. Therefore, we use a Band function to fit the GBM-only data for this interval, and the best-fit results are $E_{\text{peak}} = 321.08_{-166.05}^{+368.28}$ MeV, $\alpha = -1.24_{-0.12}^{+0.16}$ and $\beta = -1.72_{-0.10}^{+0.06}$. The large value of β could be due to that the GBM emission contains some contribution from the afterglow emission. The preferred νF_ν model spectra for each time bins considered in the time-resolved spectroscopy are shown in Figure 4. The results of the model parameters are summarized in Table 2.

5. THE LAT EXTENDED EMISSION

We show the light curve of GRB 240825A in the energy band 0.1–100 GeV in Figure 5, assuming a power-law spectrum for the data in the analysis. One can note that, the light curve shows intense variability during the early phase when the prompt MeV emission is strong and after that the flux decays monotonously in time. The decay seems to be composed by two phases, an initial steep decay and then a shallow one at late times. Motivated by this, we study whether a break in the light curve can be revealed from the LAT data. We use a broken power-law model to fit the data points after $T_0 + 3.9$ s (see the top panel in Figure 5). The best-fitting result gives a slope of $\lambda_1 = -5.39_{-2.11}^{+2.21}$ before the break and a slope of $\lambda_2 = -1.08_{-0.25}^{+0.15}$ after the break, and a break time at $t_b = T_0 + (6.16_{-1.25}^{+1.62})$ s. The broken power-law model fit yields $\chi^2/\text{dof} = 2.45/7$, while the single power-law model yields $\chi^2/\text{dof} = 8.37/7$, indicating that the broken power-law model fits the data better than the single power-law model. The late-time decay slope $-1.08_{-0.25}^{+0.15}$ is similar to those of other LAT-detected GRBs, such as GRB 090510, GRB 090902B and GRB 090926A (Abdo et al. 2009c,d; Ackermann et al. 2011).

We model the LAT emission spectrum as a power law, and the spectral indices of each intervals are shown in the bottom panel of Figure 5. We find that the spectral index shows significant variation during the early prompt emission phase. During the steep decay phase, the spectrum becomes soft with time. Finally, the spectral index stabilize at ~ -2 at late times, indicating the afterglow origin for this phase.

6. DISCUSSION AND INTERPRETATION

6.1. Interpretation of the extra hard component

It has been proposed that the extra hard component could be attributed to the external shock, which is made by the interaction of the jet with the ambient medium, and the onset delays of GeV emission corresponds to the times for the jet deceleration (Kumar & Barniol Duran 2009; Ghisellini et al. 2010). However, the emission of the extra hard component of GRB 240825A has a strong variability and it correlates with the MeV emission in time, which is at odds with an external shock origin. The spectral slopes below and above the peak of the extra components in GRB 240825A are also inconsistent with afterglow synchrotron emission.

Within the internal shock synchrotron scenario, an extra component could be produced by the synchrotron self-Compton (SSC) emission. The electrons are assumed to have a power-law spectrum $dn/d\gamma_e \propto \gamma_e^{-p}$ above a minimum Lorentz factor of γ_m at the injection. The peak energy of the extra component at ~ 50 MeV would require a Lorentz factor $\gamma_m = (\nu_{\text{SSC}}/\nu_{\text{syn}})^{1/2} \sim 11$ for the electrons, assuming a SSC peak at $h\nu_{\text{SSC}} = 51$ MeV and a synchrotron peak at $h\nu_{\text{syn}} = 360$ keV for GRB 240825A. In order to have the synchrotron emission peaking at $h\nu_{\text{syn}} = 360$ keV, such a low γ_m would require an extremely large magnetic field, $B = 4 \times 10^9 \text{G} (\Gamma/300)^{-1}$, where Γ is the bulk Lorentz factor of the relativistic jet. Assuming a fraction of ϵ_B of the jet kinetic luminosity L_k entering in the magnetic field, we have $B^2/8\pi = \epsilon_B L_k / (4\pi R^2 \Gamma^2 c)$, where R is the radius of the internal shock. It leads to a small radius $R \sim 10^{10} \text{cm} \epsilon_B^{1/2} L_{k,54}^{1/2}$, which is unreasonable for an optically thin internal shock. Thus, the low peak of the extra hard component challenges the synchrotron plus SSC emission model for the prompt emission of GRB 240825A.

In the photospheric emission model of the Band component (e.g., Mészáros & Rees 2000), the extra component could result from the IC scattering of the photospheric emission by relativistic electrons in the internal shock/dissipation region at large radius above the photosphere (Beloborodov 2009; Gao et al. 2009; Ryde et al. 2010; Toma et al. 2011). The Lorentz factor of relativistic electrons accelerated in the internal shock is expected to be $\gamma_m = \frac{\epsilon_e}{\eta_{\pm}} \frac{m_p}{m_e} \frac{p-2}{p-1} (\Gamma_{sh} - 1)$, where Γ_{sh} is the Lorentz factor of internal shock, ϵ_e is the fraction of the dissipation energy that is carried by electrons, and η_{\pm} is the number of e^{\pm} pairs for one baryon in the jet. The value of $\gamma_m = 11$ implies $\eta_{\pm} \sim 6(\epsilon_e/0.1)^{-1}$ for a mildly internal shock with $\Gamma_{sh} \sim 2$ and $p \sim 2.5$. These pairs may be created by dissipation in the photosphere region (Toma et al. 2011).

In the above discussion, we have assumed that the peak of the extra hard components in GRB 240825A represents an intrinsic spectral break related to the energy distribution of the emitting particles or the emission mechanism, rather than the $\gamma\gamma$ absorption effect. It has been argued that, although the instantaneous emission from a thin shell exhibits a photon spectrum with an exponential cutoff, the shape of the time-integrated spectrum of a single pulse may depend on the details of the emission mechanism and could be a broken power-law (Granot et al. 2008). However, taking the break in GRB 240825A as the absorption break would imply that the intrinsic peak energy is higher and the energy budget in the extra component becomes correspondingly higher (i.e. the Compton parameter $Y \gg 1$). Although we can not rule out this possibility, we disfavor this scenario from the viewpoint of the energy budget.

6.2. Temporally extended GeV emission

The late smooth decay of GRB 240825A with a temporal slope of ~ -1 is similar to the temporally extended emission seen in other LAT GRBs. This smooth decay arises naturally from the afterglow emission. A remarkable new feature seen in the extended GeV emission of GRB 240825A is the steep decay between the early variable prompt emission and the late extended emission. Although the steep decay has been commonly seen in the X/gamma-ray emission at the end of the prompt emission, it is seen for the first time in the GeV band. We interpret this steep decay in the GeV band as the high latitude emission of the relativistic jet (Kumar & Panaitescu 2000), similar to the origin of the steep decay in X/gamma-ray emission. The decay slope of the high-latitude emission is $t^{-(2+\beta)}$, where β is the spectral index of the flux density (i.e., $F_{\nu} \propto \nu^{-\beta}$). With $\beta \sim 1.5$, we expect a decay of $t^{-3.5}$, which is consistent with the observation. The simultaneous spectral softening during this phase supports this interpretation, as the GeV spectrum usually becomes softer towards higher energies. Therefore we see a clear transition from the prompt emission phase to the afterglow in the GeV emission of GRB 240825A.

7. SUMMARY

By analyzing the *Fermi* GBM and LAT data of GRB 240825A, we find a two-hump structure in the spectrum of the prompt emission. The low energy component can be described by the usual Band function, while the high-energy component can be described by a broken power-law with a break at about 50 MeV. We also find that the broken power-law model fits the spectral data of the high-energy component better than the cutoff power-law

model in the time-resolved spectrum during the second emission pulse. This suggests that the break could be an intrinsic peak of the extra component. In this case, the peak energy could put useful constraints on the radiation mechanism for the prompt emission. In particular, we find that the low ratio between the two peaks implies a very low γ_m in the synchrotron plus SSC scenario for the two-hump spectrum. Such a low γ_m requires an unreasonably large magnetic field to produce the synchrotron emission peaking at hundreds of keV, challenging the

synchrotron model for the Band component. On the other hand, the photosphere model does not have such constraint, and inverse-Compton scattering of the photosphere emission could be a viable explanation for the extra component in GRB 240825A.

- 1 The work is supported by the NSFC under grants Nos.
- 2 12333006, 12203022, 12121003.

REFERENCES

- Abdo, A. A., Ackermann, M., Asano, K., et al. 2009a, *ApJ*, 707, 580, doi: [10.1088/0004-637X/707/1/580](https://doi.org/10.1088/0004-637X/707/1/580)
- Abdo, A. A., Ackermann, M., Arimoto, M., et al. 2009b, *Science*, 323, 1688, doi: [10.1126/science.1169101](https://doi.org/10.1126/science.1169101)
- Abdo, A. A., Ackermann, M., Ajello, M., et al. 2009c, *Nature*, 462, 331, doi: [10.1038/nature08574](https://doi.org/10.1038/nature08574)
- . 2009d, *ApJL*, 706, L138, doi: [10.1088/0004-637X/706/1/L138](https://doi.org/10.1088/0004-637X/706/1/L138)
- . 2010, *ApJ*, 712, 558, doi: [10.1088/0004-637X/712/1/558](https://doi.org/10.1088/0004-637X/712/1/558)
- Ackermann, M., Ajello, M., Baldini, L., et al. 2010a, *ApJL*, 717, L127, doi: [10.1088/2041-8205/717/2/L127](https://doi.org/10.1088/2041-8205/717/2/L127)
- Ackermann, M., Asano, K., Atwood, W. B., et al. 2010b, *ApJ*, 716, 1178, doi: [10.1088/0004-637X/716/2/1178](https://doi.org/10.1088/0004-637X/716/2/1178)
- Ackermann, M., Ajello, M., Asano, K., et al. 2011, *ApJ*, 729, 114, doi: [10.1088/0004-637X/729/2/114](https://doi.org/10.1088/0004-637X/729/2/114)
- Arnaud, K. A. 1996, in *Astronomical Society of the Pacific Conference Series*, Vol. 101, *Astronomical Data Analysis Software and Systems V*, ed. G. H. Jacoby & J. Barnes, 17
- Asano, K., Guiriec, S., & Mészáros, P. 2009, *ApJL*, 705, L191, doi: [10.1088/0004-637X/705/2/L191](https://doi.org/10.1088/0004-637X/705/2/L191)
- Atwood, W. B., Abdo, A. A., Ackermann, M., et al. 2009, *ApJ*, 697, 1071, doi: [10.1088/0004-637X/697/2/1071](https://doi.org/10.1088/0004-637X/697/2/1071)
- Band, D., Matteson, J., Ford, L., et al. 1993, *ApJ*, 413, 281, doi: [10.1086/172995](https://doi.org/10.1086/172995)
- Beloborodov, A. M. 2009, *ApJ*, 703, 1044, doi: [10.1088/0004-637X/703/1/1044](https://doi.org/10.1088/0004-637X/703/1/1044)
- Bošnjak, Ž., & Daigne, F. 2014, *A&A*, 568, A45, doi: [10.1051/0004-6361/201322341](https://doi.org/10.1051/0004-6361/201322341)
- Brivio, R., Ferro, M., D’Avanzo, P., et al. 2024, *GRB Coordinates Network*, 37295, 1
- Burgess, J. M., Kole, M., Berlato, F., et al. 2019, *A&A*, 627, A105, doi: [10.1051/0004-6361/201935056](https://doi.org/10.1051/0004-6361/201935056)
- Burgess, J. M., Preece, R. D., Connaughton, V., et al. 2014, *ApJ*, 784, 17, doi: [10.1088/0004-637X/784/1/17](https://doi.org/10.1088/0004-637X/784/1/17)
- Cheng, Y., Pan, Y., Yang, Y.-P., et al. 2024, *arXiv e-prints*, arXiv:2409.14716, doi: [10.48550/arXiv.2409.14716](https://doi.org/10.48550/arXiv.2409.14716)
- Daigne, F., Bošnjak, Ž., & Dubus, G. 2011, *A&A*, 526, A110, doi: [10.1051/0004-6361/201015457](https://doi.org/10.1051/0004-6361/201015457)
- Di Lalla, N., Gupta, R., Holzmann, A., & Fermi-LAT Collaboration. 2024, *GRB Coordinates Network*, 37288, 1
- Dutton, D., Dubay, M., Schlegel, D., et al. 2024, *GRB Coordinates Network*, 37276, 1
- Evans, P. A., Goad, M. R., Osborne, J. P., Beardmore, A. P., & Swift-XRT Team. 2024, *GRB Coordinates Network*, 37290, 1
- Fermi GBM Team. 2024, *GRB Coordinates Network*, 37273, 1
- Frederiks, D., Lysenko, A., Ridnaia, A., et al. 2024, *GRB Coordinates Network*, 37302, 1
- Gao, H., & Zhang, B. 2015, *ApJ*, 801, 103, doi: [10.1088/0004-637X/801/2/103](https://doi.org/10.1088/0004-637X/801/2/103)
- Gao, W.-H., Mao, J., Xu, D., & Fan, Y.-Z. 2009, *ApJL*, 706, L33, doi: [10.1088/0004-637X/706/1/L33](https://doi.org/10.1088/0004-637X/706/1/L33)
- Ghisellini, G., Ghirlanda, G., Nava, L., & Celotti, A. 2010, *MNRAS*, 403, 926, doi: [10.1111/j.1365-2966.2009.16171.x](https://doi.org/10.1111/j.1365-2966.2009.16171.x)
- Granot, J., Cohen-Tanugi, J., & Silva, E. d. C. e. 2008, *ApJ*, 677, 92, doi: [10.1086/526414](https://doi.org/10.1086/526414)
- Guiffreda, O., Durbak, J., Atri, S., et al. 2024, *GRB Coordinates Network*, 37303, 1
- Gupta, R., Brivio, R., Dichiaro, S., et al. 2024, *GRB Coordinates Network*, 37274, 1
- Jiang, S. Q., Liu, X., An, J., et al. 2024, *GRB Coordinates Network*, 37275, 1
- Kumar, P., & Barniol Duran, R. 2009, *MNRAS*, 400, L75, doi: [10.1111/j.1745-3933.2009.00766.x](https://doi.org/10.1111/j.1745-3933.2009.00766.x)
- Kumar, P., & Panaitescu, A. 2000, *ApJL*, 541, L9, doi: [10.1086/312888](https://doi.org/10.1086/312888)
- Kumar, P., & Zhang, B. 2015, *PhR*, 561, 1, doi: [10.1016/j.physrep.2014.09.008](https://doi.org/10.1016/j.physrep.2014.09.008)
- Li, R. Z., Wang, B. T., Song, F. F., et al. 2024, *GRB Coordinates Network*, 37280, 1
- Lipunov, V., Kornilov, V., Gorbovskoy, E., et al. 2024, *GRB Coordinates Network*, 37279, 1

- Martin-Carrillo, A., Schneider, B., Pugliese, G., et al. 2024, GRB Coordinates Network, 37293, 1
- Meegan, C., Lichti, G., Bhat, P. N., et al. 2009, ApJ, 702, 791, doi: [10.1088/0004-637X/702/1/791](https://doi.org/10.1088/0004-637X/702/1/791)
- Mészáros, P., & Rees, M. J. 2000, ApJ, 530, 292, doi: [10.1086/308371](https://doi.org/10.1086/308371)
- Nava, L. 2018, International Journal of Modern Physics D, 27, 1842003, doi: [10.1142/S0218271818420038](https://doi.org/10.1142/S0218271818420038)
- Nunes, R. C., Pan, S., Saridakis, E. N., & Abreu, E. M. C. 2017, JCAP, 2017, 005, doi: [10.1088/1475-7516/2017/01/005](https://doi.org/10.1088/1475-7516/2017/01/005)
- Odeh, M., & Guessoum, N. 2024, GRB Coordinates Network, 37277, 1
- Pe'er, A., & Zhang, B. 2006, ApJ, 653, 454, doi: [10.1086/508681](https://doi.org/10.1086/508681)
- Ravasio, M. E., Salafia, O. S., Oganesyan, G., et al. 2024, Science, 385, 452, doi: [10.1126/science.adj3638](https://doi.org/10.1126/science.adj3638)
- Ryde, F., Axelsson, M., Zhang, B. B., et al. 2010, ApJL, 709, L172, doi: [10.1088/2041-8205/709/2/L172](https://doi.org/10.1088/2041-8205/709/2/L172)
- Schwarz, G. 1978, Annals of Statistics, 6, 461
- Sharma, V., Meegan, C., & Fermi Gamma-ray Burst Monitor Team. 2024, GRB Coordinates Network, 37301, 1
- SVOM/C-GFT Team, Wu, C., Kang, Z., et al. 2024, GRB Coordinates Network, 37292, 1
- Toma, K., Wu, X. F., & Mészáros, P. 2011, MNRAS, 415, 1663, doi: [10.1111/j.1365-2966.2011.18807.x](https://doi.org/10.1111/j.1365-2966.2011.18807.x)
- Uhm, Z. L., & Zhang, B. 2014, Nature Physics, 10, 351, doi: [10.1038/nphys2932](https://doi.org/10.1038/nphys2932)
- Wang, C.-W., Xiong, S.-L., & Gecam Team. 2024, GRB Coordinates Network, 37315, 1
- Wang, X.-Y., Li, Z., Dai, Z.-G., & Mészáros, P. 2009, ApJL, 698, L98, doi: [10.1088/0004-637X/698/2/L98](https://doi.org/10.1088/0004-637X/698/2/L98)
- Zhang, B.-B., Uhm, Z. L., Connaughton, V., Briggs, M. S., & Zhang, B. 2016, ApJ, 816, 72, doi: [10.3847/0004-637X/816/2/72](https://doi.org/10.3847/0004-637X/816/2/72)
- Zhang, J., Du, G., Guo, H., et al. 2024, GRB Coordinates Network, 37278, 1

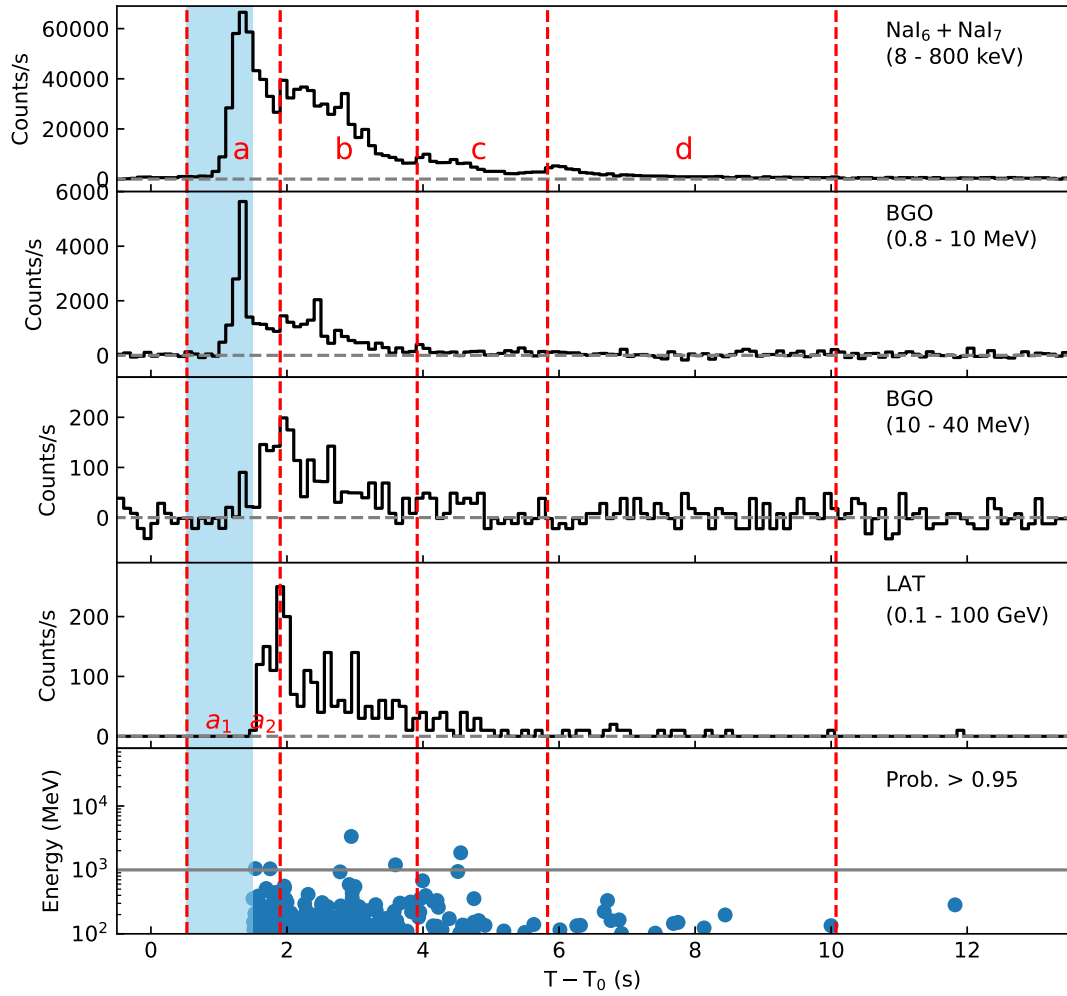


Figure 1. GBM and LAT count-rate light curves of GRB 240825A with 0.1 s time binning in different energy band. The bottom panel shows the energies of the events above 100 MeV that have high association probability ($> 95\%$) with this GRB. The dashed red vertical lines indicate the time intervals that are selected for spectral analyses and the blue shadow region indicates the time interval a_1 when no high-energy photons are detected by *Fermi* LAT.

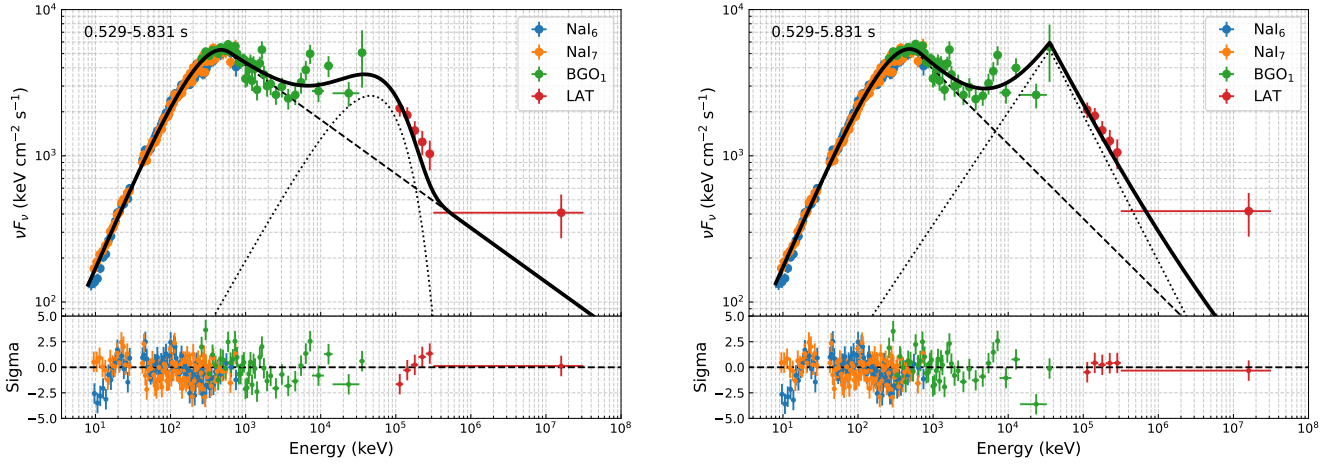


Figure 2. The time-integrated spectrum measured from $T_0 + 0.529$ s to $T_0 + 5.831$ s and the model fits for GRB 240825A. Left panel: The spectral fitting with the Band+CPL model. Right panel: The spectral fitting with the Band+BPL model. The dashed lines represent the Band component, the dotted lines represent the extra component (CPL or BPL component), and the solid lines represent the sum of them. The lower panels show the residual of the spectral fitting.

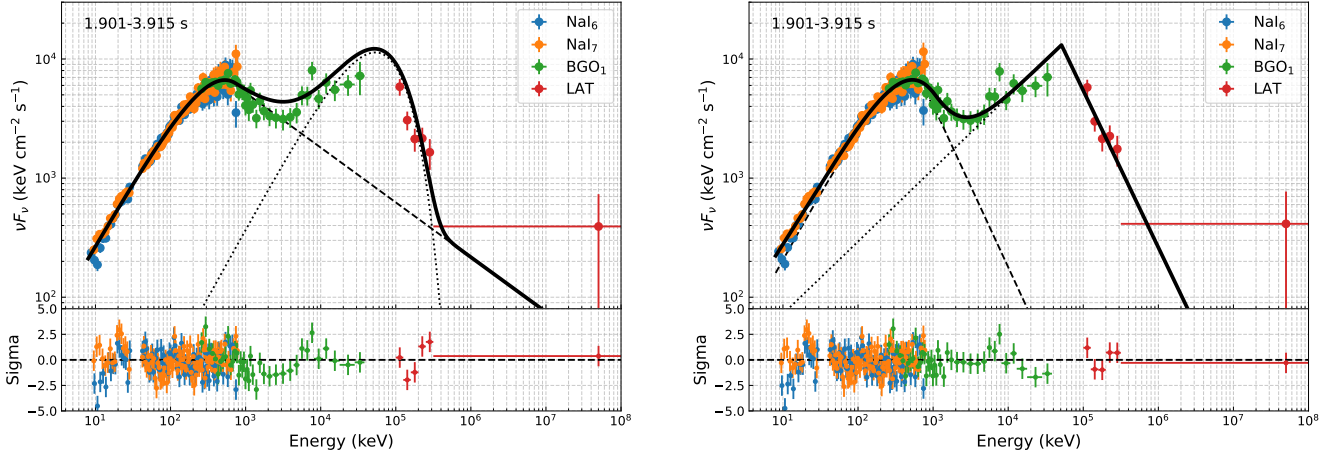


Figure 3. The time-resolved spectrum of GRB 240825A measured from $T_0 + 1.901$ s to $T_0 + 3.915$ s (interval b). Left panel: The spectral fitting with the Band+CPL model. Right panel: The spectral fitting with the Band+BPL model. The dashed lines represent the Band component, the dotted lines represent the extra component (CPL or BPL component), and the solid lines represent the sum of them. The lower panels show the residual of the spectral fitting.

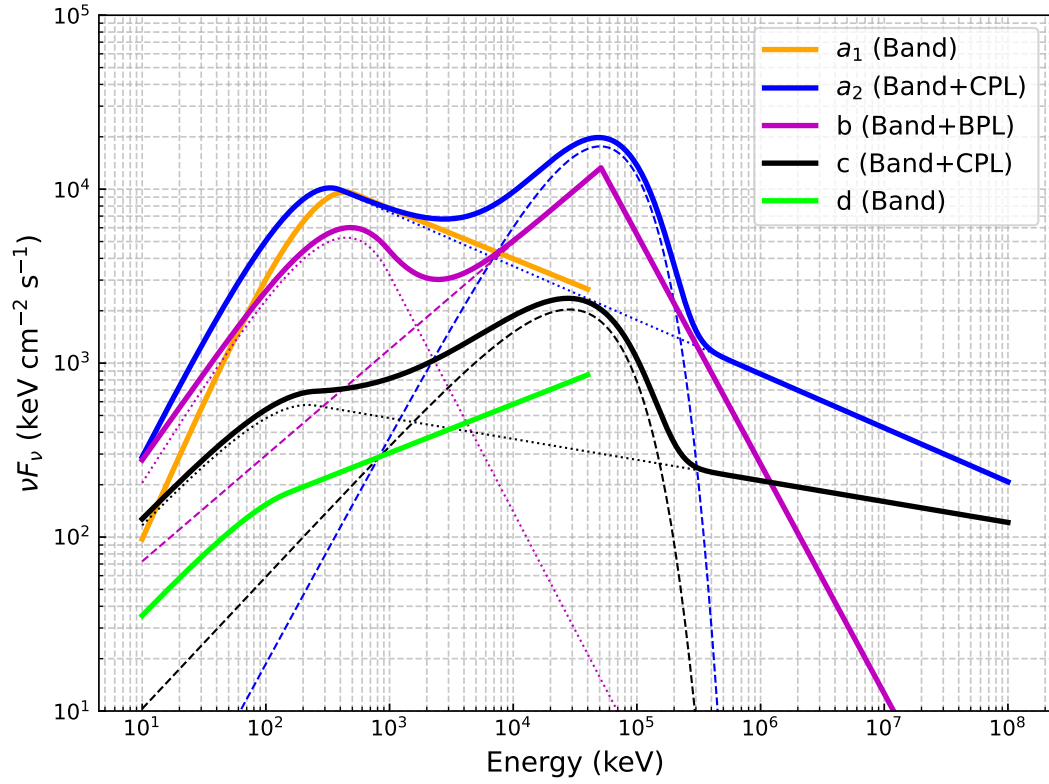


Figure 4. The νF_ν model spectra plotted for each of the time bins considered in the time-resolved spectroscopy. The dotted lines represent the Band component, the dashed lines represent the extra component (CPL or BPL component), and the solid lines represent the best-fit model.

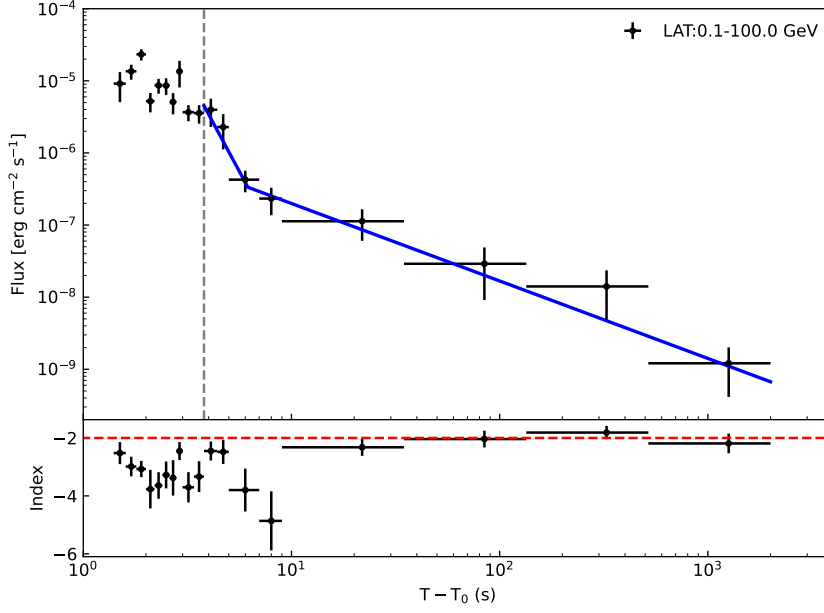


Figure 5. Time variation of the LAT flux (top panel) and photon index (bottom panel) for GRB 240825A. The blue line shows the fit with a broken power-law to the data after $T_0 + 3.9$ s.

Table 1. The GBM/LAT joint spectral fitting results for the interval $T_0 + [0.529, 5.831]$ s.

Fitting model	Band	Band+CPL	Band+BPL
<i>Band</i>			
A (photons $\text{cm}^{-2} \text{s}^{-1} \text{keV}^{-1}$)	0.275 ± 0.005	$0.272^{+0.005}_{-0.007}$	$0.152^{+0.004}_{-0.004}$
α	$-0.81^{+0.02}_{-0.01}$	$-0.80^{+0.03}_{-0.02}$	$-0.80^{+0.03}_{-0.02}$
β	$-2.24^{+0.01}_{-0.02}$	$-2.37^{+0.04}_{-0.05}$	$-2.51^{+0.11}_{-0.17}$
E_{peak} (keV)	$394.26^{+15.71}_{-15.59}$	$389.15^{+22.14}_{-17.26}$	$394.89^{+19.66}_{-19.65}$
<i>CPL</i>			
B (photons $\text{cm}^{-2} \text{s}^{-1} \text{keV}^{-1}$)	-	$0.364^{+3.561}_{-0.355}$	-
α_1	-	$1.09^{+0.26}_{-0.38}$	-
E_{cut} (MeV)	-	$50.74^{+29.64}_{-16.11}$	-
<i>BPL</i>			
C (photons $\text{cm}^{-2} \text{s}^{-1} \text{keV}^{-1}$)	-	-	$1.656^{+3.715}_{-1.552}$
α_l	-	-	$-1.23^{+0.31}_{-0.12}$
α_h	-	-	$-3.00^{+0.36}_{-0.44}$
E_{break} (MeV)	-	-	$35.71^{+14.29}_{-15.08}$
PGSTAT / dof	648.41/362	574.96/359	564.82/358
BIC	672.02	616.28	612.04

Table 2. The GBM/LAT joint spectral fitting results for the time-resolved spectra.

Time intervals from T_0 (s)	(a) 0.529–1.901	(a1) 0.529–1.500	(a2) 1.500–1.901	(b) 1.901–3.915	(c) 3.915–5.831	(d) 5.831–10.072
Preferred model	Band+CPL	Band	Band+CPL	Band+BPL	Band+CPL	Band
<i>Band</i>						
A (photons $\text{cm}^{-2} \text{s}^{-1} \text{keV}^{-1}$)	$0.527^{+0.016}_{-0.015}$	$0.441^{+0.019}_{-0.017}$	$0.772 \pm +0.051$	$0.297^{+0.015}_{-0.013}$	$0.068^{+0.019}_{-0.010}$	$0.021^{+0.008}_{-0.004}$
α	-0.50 ± 0.03	-0.36 ± 0.04	-0.59 ± 0.05	$-0.85^{+0.07}_{-0.06}$	$-1.25^{+0.32}_{-0.07}$	$-1.24^{+0.16}_{-0.12}$
β	-2.38 ± 0.05	$-2.29^{+0.05}_{-0.06}$	$-2.31^{+0.10}_{-0.19}$	$-3.36^{+0.46}_{-1.24}$	$-2.12^{+0.09}_{-0.08}$	$-1.72^{+0.06}_{-0.10}$
E_{peak} (keV)	$274.64^{+14.84}_{-15.27}$	$266.81^{+18.33}_{-17.52}$	$232.96^{+24.47}_{-22.35}$	$388.74^{+42.27}_{-39.61}$	$289.83^{+134.05}_{-174.22}$	$321.08^{+368.28}_{-166.05}$
<i>CPL</i>						
B (photons $\text{cm}^{-2} \text{s}^{-1} \text{keV}^{-1}$)	$0.356^{+2.385}_{-0.179}$	-	$0.045^{+1.762}_{-0.013}$	-	$1.79^{+15.88}_{-0.64}$	-
α_1	$-1.04^{+0.60}_{-0.21}$	-	$-0.69^{+0.58}_{-0.39}$	-	$-1.24^{+0.27}_{-0.49}$	-
E_{cut} (MeV)	$42.98^{+16.16}_{-13.78}$	-	$38.58^{+17.89}_{-12.09}$	-	$37.49^{+20.08}_{-15.01}$	-
<i>BPL</i>						
C (photons $\text{cm}^{-2} \text{s}^{-1} \text{keV}^{-1}$)	-	-	-	$17.790^{+15.754}_{-3.766}$	-	-
α_2	-	-	-	$-1.39^{+0.07}_{-0.12}$	-	-
α_3	-	-	-	$-3.32^{+0.32}_{-0.31}$	-	-
E_{break} (MeV)	-	-	-	$51.22^{+12.19}_{-12.68}$	-	-
<i>PGSTAT / dof</i>						
Band	409.04/363	377.16/333	434.38/363	585.68/363	455.69/363	409.51/333
Band+CPL	386.84/360	-	356.95/360	463.70/360	409.19/360	396.13/330
Band+BPL	386.98/359	-	355.76/359	442.79/359	408.84/359	-
ΔBIC						
Band \rightarrow (Band+CPL)	4.48	-	59.71	104.26	28.78	-4.08
(Band+CPL) \rightarrow (Band+BPL)	-6.04	-	-4.71	15.00	-5.55	-